ORBIT TOPOLOGY IN CONVENTIONAL STELLARATORS IN THE PRESENCE OF ELECTRIC FIELDS

JAMES A. ROME
Oak Ridge National Laboratory,
Oak Ridge, Tennessee, United States of America

ABSTRACT. Orbits are considered in conventional stellarators (i.e. with helical coils) using Boozer co-ordinates. The Advanced Toroidal Facility (ATF) in Oak Ridge, Tennessee, will be used as an example to study the effects of its configurational flexibility on orbit topology. It is shown that the symplectic integration technique yields superior results for single particle orbits. These orbits will be compared with predictions using the J^* invariant. J^* conservation allows examination and understanding of the global stellarator topology, both with and without radial electric fields.

1. INTRODUCTION

The inherently three dimensional nature of stellarators causes a wide variety of orbits to occur in these devices. Knowledge of single particle confinement is required to assess confinement and alpha heating. However, in conventional stellarators such as the Advanced Toroidal Facility (ATF) torsatron, radial electric fields can have a dramatic effect on orbits with energies on the order of the radial potential. The effect of electric fields is larger in stellarators than in tokamaks because the poloidal drift of helically trapped particles is much slower, thus allowing the $\boldsymbol{E}\times\boldsymbol{B}$ drift time to have an effect. Conversely, the 'banana width' in a stellarator (the bounce in the helical well) is much smaller than in a tokamak because the distance between the bounces is only $\sim 2\pi R_0/N$, where R_0 is the major radius of the device and N is the number of field periods.

The situation can be somewhat different for stellarators that are not based upon helical coils, such as the Helias devices invented at the Max-Planck-Institut für Plasmaphysik in Garching [1]. In principle, the orbits in a Helias can achieve an effective helical symmetry (become quasi-helical). In this circumstance, the $1/R$ variation in the magnetic field due to toroidal effects becomes very small. As a result, the orbit deviation from a flux surface is reduced, and most of the effects discussed in this paper do not apply.

It is the aim of this paper to show that by using a variation of the second adiabatic invariant, J^*, introduced by Cary, Hedrick and Tolliver [2], we can quickly and easily determine the topology of all orbits in conventional stellarators for a given magnetic configuration. To show that J^* yields the correct answer, we will start by examining single particle orbits and their relation to $J^* = const.$ contours. Then we will follow in the spirit of the tokamak topology study by Rome and Peng [3] in an attempt to give an overview of all possible orbits given only the equilibrium configuration.

2. SINGLE PARTICLE ORBITS

The advantages of using Boozer co-ordinates [4–6] are well known. Knowledge of the Fourier spectrum of $|\boldsymbol{B}|$, and other surface quantities (the rotational transform ι, the toroidal current within a flux surface I, the poloidal current outside a flux surface g) suffice to specify completely the orbit topology within the last closed flux surface (LCFS). We will also use Boozer's equations of motion [4, 6].

In this paper, the Boozer co-ordinates are calculated using the output of the VMEC free boundary equilibrium code [7]. Three real ATF equilibrium configurations were used to test the effect of the flexibility of the ATF vertical field coil set [8]. The cases are called *standard*, *oblate* and *prolate* to reflect the variation of the poloidal cross-section from the normal (standard) case. The parameters and coil currents for these cases are more fully described in Table I. One of our goals will be to see how changing the shape of the plasma affects orbit topology.

TABLE I. ATF EQUILIBRIUM REFERENCE CASES

Parameter	Standard	Oblate	Prolate
Helical-coil current (kA)	−823.9	−826.7	−828.8
Outer trim/ helical current ratio	-8.90×10^{-2}	-4.4×10^{-2}	-1.2×10^{-1}
Inner trim/ helical current ratio	1.26×10^{-1}	2.36×10^{-1}	5.33×10^{-2}
Mid trim/ helical current ratio	-4.06×10^{-1}	-1.33×10^{-1}	1.33×10^{-1}
$\psi(r/a=1)$	−0.215	−0.215	0.211
B_T (T)	0.942	0.945	0.947
$\iota\ (r/a=1)$	0.99	0.96	0.97
beta (%)	0.481	0.386	0.421

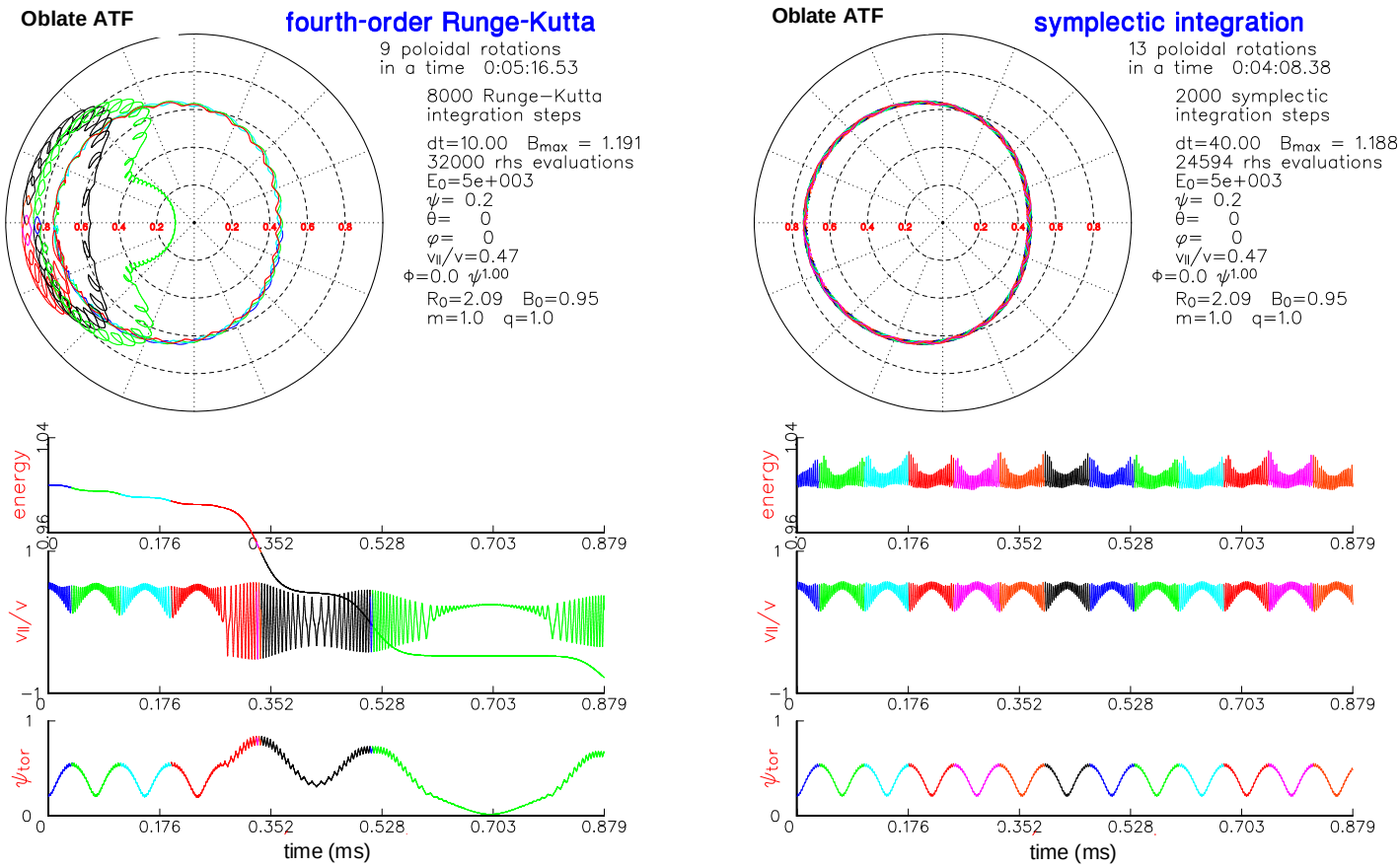

FIG. 1. The same collisionless orbit in ATF was integrated by two different methods, fourth order Runge–Kutta (left) and Cary's second order symplectic method (right). The time step in the Runge–Kutta method was halved until the number of evaluations of the right hand side of the equations was greater than that of the symplectic method. The Runge–Kutta integrator shows a monotonic reduction in the particle's energy, which is caused by a reduction in $v_\parallel/v$ *that causes the orbit to become trapped. On the other hand, with the symplectic integrator, the energy varies periodically along the orbit, but there is no long-term degradation. The magnitude of this periodic change in the energy is proportional to the time step.*

The numerical techniques used for orbit integration deserve some discussion. In recent years, the technique of symplectic integration has been introduced to plasma physics by Cary [9], whose second-order symplectic integrator we will use. The basis for Symplectic integration is to find a way such that the Hamiltonian equations of motion at time $t + \delta t$ are a canonical transformation of the equations at time t. The integrator is the generating function of this transformation. As a result, all of the Poincaré invariants are exactly conserved (to machine accuracy).

When comparing orbits integrated using symplectic integration with orbits integrated using other techniques (e.g., Runge–Kutta, ODE, Bulirisch–Stoer), the symplectic method will always be more accurate over the long term because all of the other methods have monotonic changes in the energy of collisionless orbits. Figure 1 shows a comparison of the same orbit integrated using the symplectic method and the fourth order Runge–Kutta (RK) method with the time step halved until the number of right hand side (rhs) evaluations are about the same. Although the RK method actually uses a smaller time step and more function evaluations, the result is incorrect. Smaller time steps, variable time steps, and subtraction of the error in each step could all be used to improve the short term accuracy of conventional methods. But over long time-scales, the symplectic method will always yield a better result.

The symplectic method does have some drawbacks. It must use a fixed time step since it relies upon the error in the method to cancel itself periodically. Changing the time step makes the method non-symplectic. In addition, it is an implicit method, so it requires a fast method for inverting the rhs. Cary also has developed a fourth order symplectic method for the guiding centre equations but, in general, it seems to give worse results than the much simpler second order method.

3. THE J^* ADIABATIC INVARIANT

In Boozer co-ordinates, the toroidal canonical angular momentum is

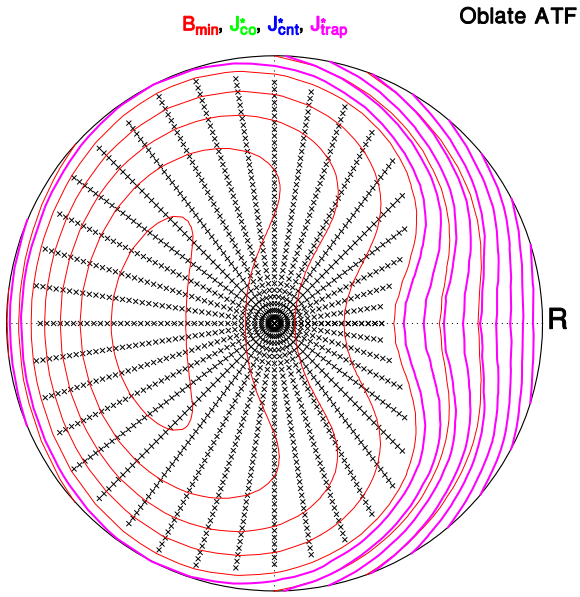

FIG. 2. J* *(thick) and* B_{min} *(thin) contours for the case corresponding to Fig. 3. The grid points marked by* × *are in a region where* $B_{min} > B_{tip}$ *and is therefore inaccessible to these orbits. The edge of this region is the* B_{min} *contour that corresponds to the orbits shown in Fig. 3. Most of the* J* *contours intersect the LCFS and correspond to orbits that are lost.*

$$P_\varphi = e\,[g(\psi)\rho_c - \psi_p] \tag{1}$$

where $\rho_c \equiv m v_{||}/eB$ and the parallel velocity is given by

$$v_{||} = \pm\left[\frac{2}{m}(E - \mu B - e\Phi)\right]^{1/2} \tag{2}$$

Here, e, m and E are the charge, mass and total energy of the particle, ψ is the toroidal flux, ψ_p is the poloidal flux, μ is the magnetic moment, Φ is the radial potential, B is the magnitude of the magnetic field and $v_{||}$ is the parallel velocity.

The usual adiabatic invariant J is defined as the integral of P_φ along the trapped orbit between turning points (places where $v_{||} = 0$). J^* applies to trapped or untrapped particles and is defined as the integral over a field period along a $\psi = const.$, $\theta = const.$ line. The integration is only carried out for the portion of the field period where $v_{||}^2 \geq 0$. θ is the poloidal angle in Boozer co-ordinates [2]. The result of the integration is

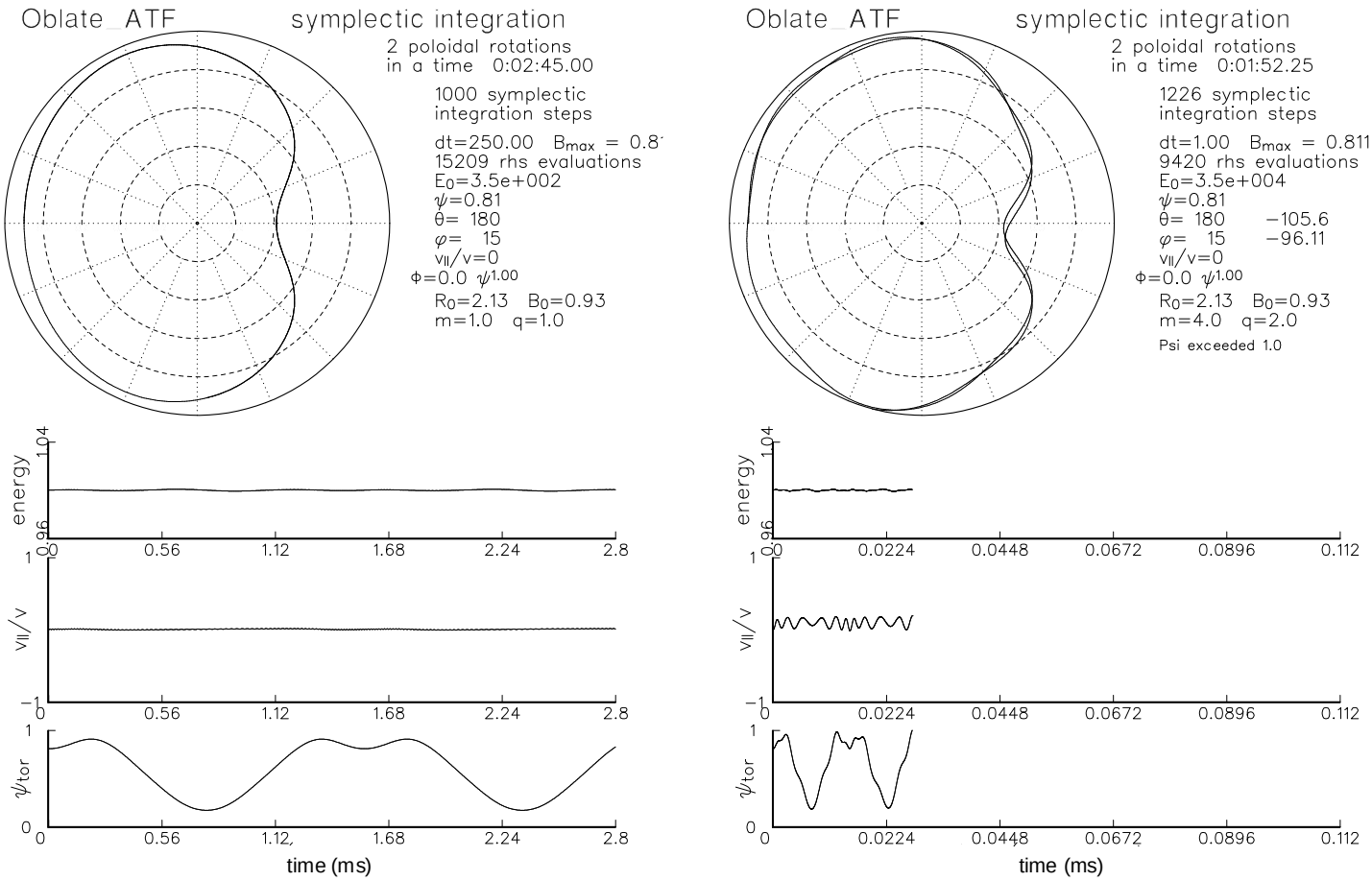

FIG. 3. Orbits with J* = 0 *approximately follow contours of* B_{min} *independent of mass, charge and energy. On the left is a 350 eV proton orbit and on the right a 35 keV alpha orbit. The 'centre' of the alpha orbit is the same as the low energy proton orbit. However, since* J* *is only an adiabatic invariant, the actual orbit will wobble about the* J* *contour, and this wobble gets larger with energy. Because the Boozer co-ordinate representation of the ATF magnetic field stops at the LCFS, the integration of the alpha orbit is stopped when it reaches the LCFS. However, in the actual machine, orbits can extend well past the LCFS without hitting the wall. For the ATF configuration,* $v_{||} > 0$ *corresponds to the counter-circulating portion of the orbit.*

$$J^*(\psi,\theta)=\int_{\psi,\theta=const}\frac{g(\psi)d\varphi}{B}m|v_{||}|-\sigma_{||}e\frac{2\pi}{N}\psi_p \qquad (3)$$

N is the number of field periods, $\sigma_{||}$ is the sign of $v_{||}$ for locally untrapped particles and $\sigma_{||} = 0$ for locally trapped particles. By locally trapped, we mean that $v_{||} = 0$ along the line of integration. For convenience, we have attached the $\pm$ sign on the second term and divided J^* by two for trapped particles.

For locally trapped particles, the second term of Eq. (3) cancels since the integral must be taken along both halves of the orbit. In this case, and in the limit of small rotational transform per period, J^* reduces to the usual adiabatic invariant, J. For deeply trapped particles, $v_{||} \sim 0$, and the J^* = *const.* contours lie along B_{min} contours.

B_{min} contours are often used for quick evaluation of stellarator configurations, so they are worth exploring in some detail. To calculate the B_{min} contours, a grid of lines is selected to cover the poloidal cross-section. The minimum value of B is found in a field period, keeping ψ and θ constant. A contour plot of these values yields the orbits of the most deeply helically trapped particles. Since it is thought that these orbits have the biggest excursion from a flux surface, the ratio of the area of the largest contained B_{min} contour to the area of the LCFS is a measure of the goodness of the particle containment of the configuration. If this ratio approaches 1, the orbits are said to be 'omnigeneous' [10]. For the oblate configuration in ATF (Fig. 2), the area of closed B_{min} contours is maximized which would imply better orbit confinement for deeply trapped orbits.

A more surprising fact is that since these orbits are independent of anything other than the topology of B, they are independent of mass, charge and energy. Thus, if a trapped ion orbit is contained at low energies, in principle, an alpha particle orbit will also be contained at high energies. However, higher energy particles traverse these orbits much more rapidly since the drifts are proportional to the particle energy. An example of this phenomenon is shown in Fig. 3. As explained in the caption, ATF at a field of 1 T is not designed to hold alpha particles at 3.5 MeV, but the 35 keV orbit that is shown illustrates the principle that deeply trapped orbits approximately follow B_{min} contours.

Figure 2 shows the J^* contours that correspond to the orbits of Fig. 3. The thinner lines are the B_{min} contours for this case. Because these J^* contours are drawn for all orbits with $B_{tip} \equiv E/\mu = 0.811$, any region of the cross-section with $B_{min} > B_{tip}$ (shown by ×s on the grid points) is forbidden to this set of orbits. Only one J^* contour for this value of B_{tip} can correspond to a B_{min} contour, and that is the one at the edge of the forbidden region, $B_{tip} = B_{min}$.

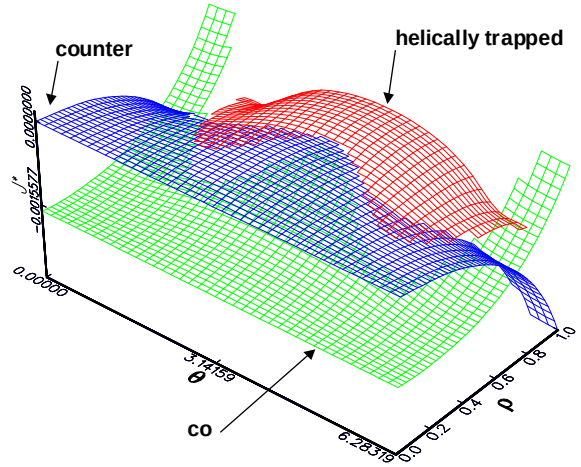

Fig. 4. Surfaces of the three sheets of J as a function of the poloidal angle and normalized radius (ρ). Each surface is only defined over part of the ρ–θ plane.*

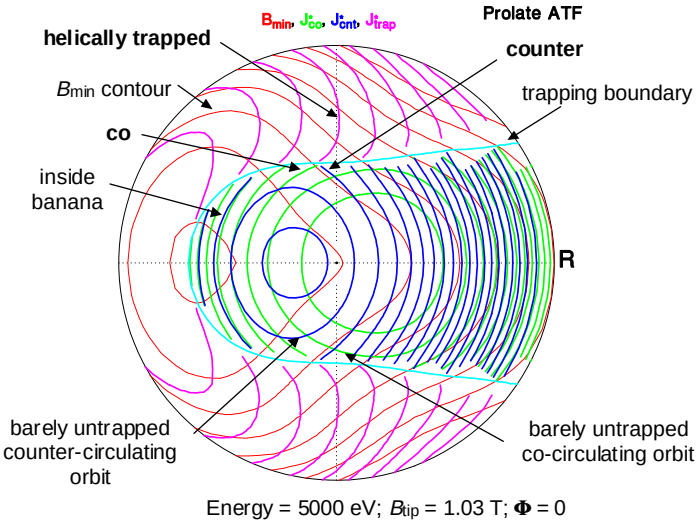

Fig. 5. Level contours of the surfaces of Fig. 4 plotted in polar co-ordinates. Because the functions stop at the trapping boundary, the contour plotter is unable to get all the way to the boundary. The bold-faced labels are attached to the three pieces of a single orbit.

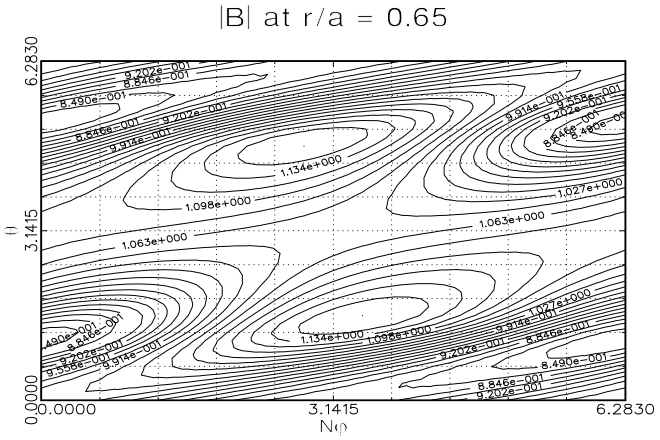

*Fig. 6. The magnetic field strength plot on a flux surface for the prolate ATF configuration. In contrast to the other two configurations, two maxima of |**B**| occur halfway down the field period instead of a single maximum at φ = 0. These maximum can trap the orbits in an unexpected location.*

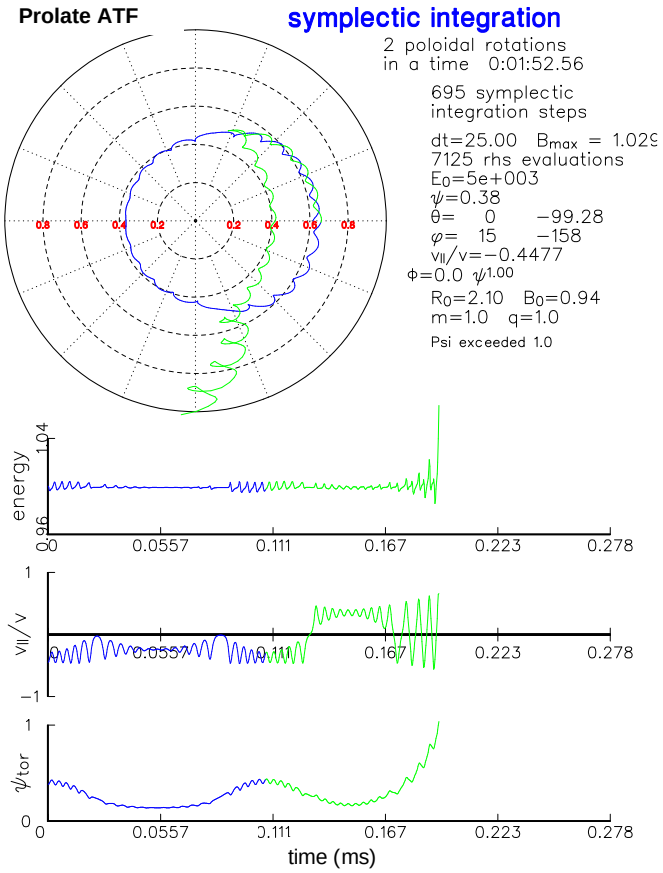

FIG. 7. A barely trapped co-orbit corresponding to the J plot of Fig. 5. In a stellarator such as ATF, the banana part of the orbit always eventually becomes helically trapped.*

4. COMPARISON OF GUIDING CENTRE ORBITS WITH THE *J** CONTOURS

In general, the *J** topology is more complicated than shown in Fig. 3 because there may be regions of the plasma in which the orbits are not locally trapped. According to Eq. (3), *J** for a given orbit will in general be constant for each phase of the orbit (locally trapped, co-circulating, counter-circulating), but will undergo a jump when the trapping boundary is crossed. If an orbit crosses the trapping boundary, the three pieces of *J** = *const.* contours that meet at the trapping boundary (on the orbit) must be used to obtain the entire orbit.

To understand some of the more pathological orbit topology that may be encountered in ATF, we consider the prolate configuration (Figs 4–6). Figure 4 shows the three *J** surfaces corresponding to the three values of $\sigma_{||}$ of Eq. (3). The discontinuity (jump in *J**) occurs at the trapping boundary. Figure 5 shows level contours of the surfaces in Fig. 4 plotted in polar co-ordinates. Since the contour levels are arbitrary, it may be necessary to interpolate between adjacent contours of a given type to determine the orbit on the other side of the trapping boundary. However, in this case, the three pieces of one orbit (with bold faced labels in Fig. 5) all meet at one point on the trapping boundary, and it is easier to see the orbit. This particular orbit is a transitional orbit that goes out past the LCFS and is lost.

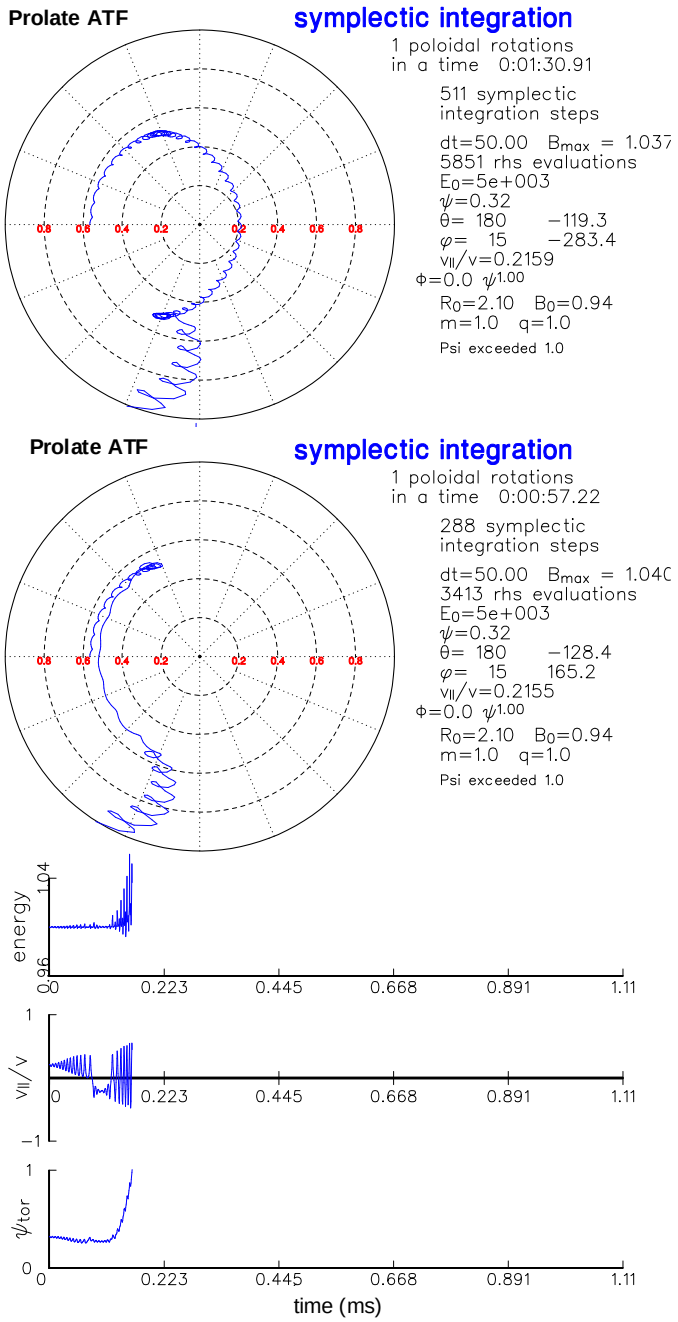

FIG. 8. Barely trapped initially counter-orbits corresponding to the J plot of Fig. 5. The initial value of $v_{||}/v$ is just slightly different to illustrate that the orbit can follow all of the branches shown in Fig. 5. In the lower case, the orbit became trapped on an inside banana, which becomes helically trapped at its next tip. In the upper case, the orbit missed the well at the top of the orbit and became helically trapped when it reached the bottom. The counter-orbits drift much more slowly than the co-orbit of Fig. 7.*

The trapping boundary will always lie along a $B_{max} = B_{tip} = const.$ contour. (B_{max} contours are calculated in the same way as B_{min} contours, using the maximum value of $|\boldsymbol{B}|$ along each ψ, $\theta = const.$ line.) The barely trapped orbit

will have its J^* contour tangent to the trapping boundary. Since this boundary may have a strange shape, barely trapped stellarator orbits do not always have their $v_{||} = 0$ point on the midplane of the stellarator. This is in contrast to the case of a tokamak.

For example, in Fig. 5, co- and counter-circulating orbits are contained near the centre of the plasma. The two orbits labelled 'barely untrapped' are just skimming over the tops of the helical ripple wells. Orbits launched slightly further from the axis hit the trapping boundary near their top and bottom, become trapped in the helical ripple well, and are lost as is shown in Figs 7 and 8. For this value of B_{tip}, all of these transitional orbits are lost. For the case of Fig. 5, a few helically trapped orbits are confined near the inside edge, and some circulating orbits are confined near the centre.

Notice that the centres of the two types of circulating orbits are shifted significantly from the magnetic axis due to the low (1 T) value of the magnetic field strength. Also, in this case, none of the orbits shown are deeply trapped since $B_{tip} > B_{min}$ everywhere; accordingly, they do not follow B_{min} contours. In a stellarator such as ATF, the three orbit classes (co-, counter-, and helically trapped) often occur in different physical locations, and the orbit traversal time may differ greatly (Figs 7 and 8), so the collisionality may be different for each class as well.

For this prolate configuration, the region of closed B_{min} contours is smallest, so orbit confinement is expected to be poor without a radial electric field. We will leave the B_{min} contours out of future plots to reduce clutter.

5. VOLUME ELEMENT IN J^* SPACE

To determine the density of orbits in J^* space, it is necessary to calculate the volume element. The use of J^* as an invariant only makes sense on time-scales that are long compared with the orbit drift time. Therefore, we assume that the particle distribution function, F, is only a function of the constants of motion, $F(J^*, E, \mu)$.

The number of particles in the distribution function is obtained by integrating over all of phase space,

$$N = \int F(J^*, E, \mu)\, \frac{2\pi \mathrm{d}E\, \mathrm{d}\mu\, \mathrm{d}\theta}{me} \int_{\psi,\, \theta = const} \frac{g + \iota I}{\rho_{||} B^2}\, \mathrm{d}\varphi \qquad (4)$$

The integral in φ is taken over the regions where $v_{||}$ is real. For simplicity we assume that $\boldsymbol{B} \cdot \nabla \times \boldsymbol{B} = 0$, in which case the guiding centre velocity may be written as

$$\boldsymbol{v}_{\mathbf{g}} = v_{||} \frac{\boldsymbol{B}}{B} + \frac{1}{B} \nabla \times (\rho_{||} \boldsymbol{B}) \qquad (5)$$

The θ component of Eq. (5) is needed to calculate the overall orbit drift velocity

$$\boldsymbol{v}_{\mathbf{g}} \cdot \nabla\theta = \frac{v_{||}}{B} \frac{B^2}{g + \iota I} [\iota + \frac{\partial}{\partial \varphi}(\beta^* \rho_{||})] \qquad (6)$$

Here β^* is the coefficient of the $\nabla\psi$ portion of the magnetic field. We also require expressions for the derivatives of J^* (the $\langle\ \rangle$ represent an average over φ):

$$\frac{\partial J^*}{\partial \psi} = -e \langle \iota - \frac{\partial}{\partial \psi}(g \rho_{||}) \rangle \qquad (7)$$

$$\frac{\partial J^*}{\partial E} = \langle \frac{g}{B v_{||}} \rangle \qquad (8)$$

In Eq. (4), we must change variables from ψ to J^*:

$$N = F(J^*, E, \mu)\, \frac{2\pi}{m^2} \frac{g + \iota I}{g} \frac{\langle \frac{\partial J^*}{\partial E} \rangle}{\langle \frac{\partial J^*}{\partial \psi} \rangle} \int \mathrm{d}J^* \mathrm{d}E \mathrm{d}\mu \mathrm{d}\theta \qquad (9)$$

The bounce averaged drift velocity is given by

$$\langle\langle \boldsymbol{v}_{\mathbf{g}} \cdot \nabla\theta \rangle\rangle = \frac{\int \frac{\mathrm{d}\varphi}{B v_{||}}\, \boldsymbol{v}_{\mathbf{g}} \cdot \nabla\theta}{\int \frac{\mathrm{d}\varphi}{B v_{||}}} \qquad (10)$$

where the integrals are performed at fixed ψ, θ. We have made use of the fact that in Boozer co-ordinates, the co-ordinate along the field line, χ, is given by $\chi = \int B \mathrm{d}l$. Using Eqs (7), (8), and (10) in Eq. (9), we obtain

$$N = F(J^*, E, \mu)\, \frac{2\pi}{m^2 e} \int \mathrm{d}J^* \mathrm{d}E \mathrm{d}\mu\, \frac{\mathrm{d}\theta}{\langle\langle \boldsymbol{v}_{\mathbf{g}} \cdot \nabla\theta \rangle\rangle} \qquad (11)$$

or

$$N = F(J^*, E, \mu)\, \frac{2\pi\tau_d}{m^2 e} \int \mathrm{d}J^* \mathrm{d}E \mathrm{d}\mu \qquad (12)$$

τ_d is the drift time around the entire orbit.

Since the distribution function for a single particle must be of the form

$$N = \int C \delta(J^* - J_0^*)\, \delta(E - E_0)\, \delta(\mu - \mu_0) \frac{2\pi\tau_d}{m^2 e} \mathrm{d}J^* \mathrm{d}E \mathrm{d}\mu$$

$$= 1 \qquad (13)$$

the constant C is given by $m^2 e / 2\pi\tau_d$, and we finally obtain the desired expression for the single-particle distribution function in this space

$$F_s(J^*, E, \mu) = \frac{m^2 e}{2\pi\tau_d}\, \delta(J^* - J_0^*)\, \delta(E - E_0)\, \delta(\mu - \mu_0) \qquad (14)$$

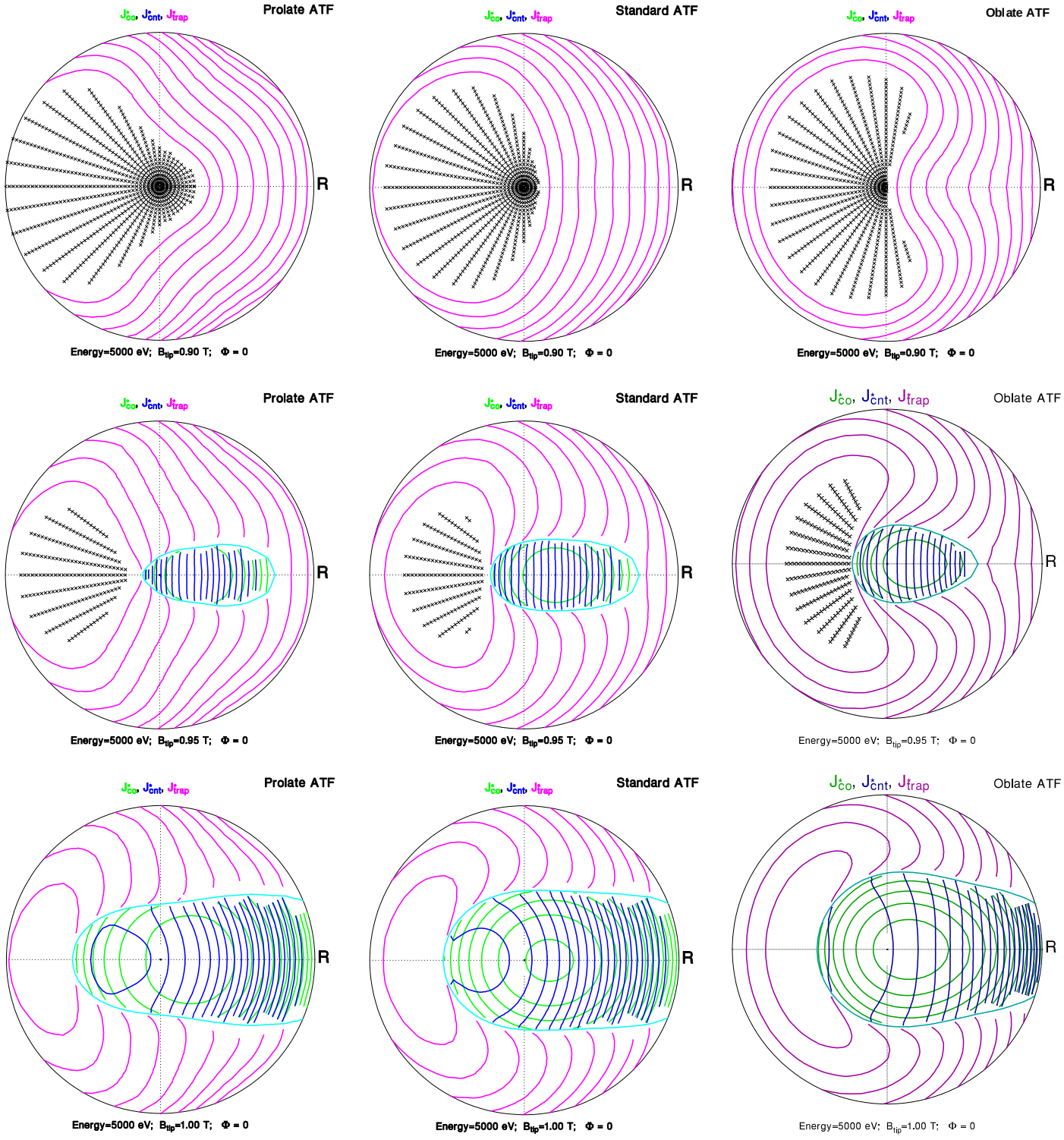

FIG. 9 (First Part). Orbit topology for 5 keV protons in ATF with no radial electric field for the three configurations of Table I.

As expected, more particles are required to populate an orbit with a large τ_d to obtain a given density at a point along the orbit in real space.

6. J^* TOPOLOGY — NO ELECTRIC FIELD

Now that the topology of J^* space has been explained and the close correspondence of the actual guiding centre orbits to their J^* predictions has been verified, it is instructive to display the entire orbit topology at a given energy for the three different ATF equilibria in the absence of radial electric fields. Because each plot is parametrized by the value $B_{tip} = E/\mu$, B_{tip} ranges from B_n, the minimum value of B in the plasma, upward. Because the topology of the circulating orbits is relatively independent of B_{tip}, it is not necessary to go much above B_m, the maximum value

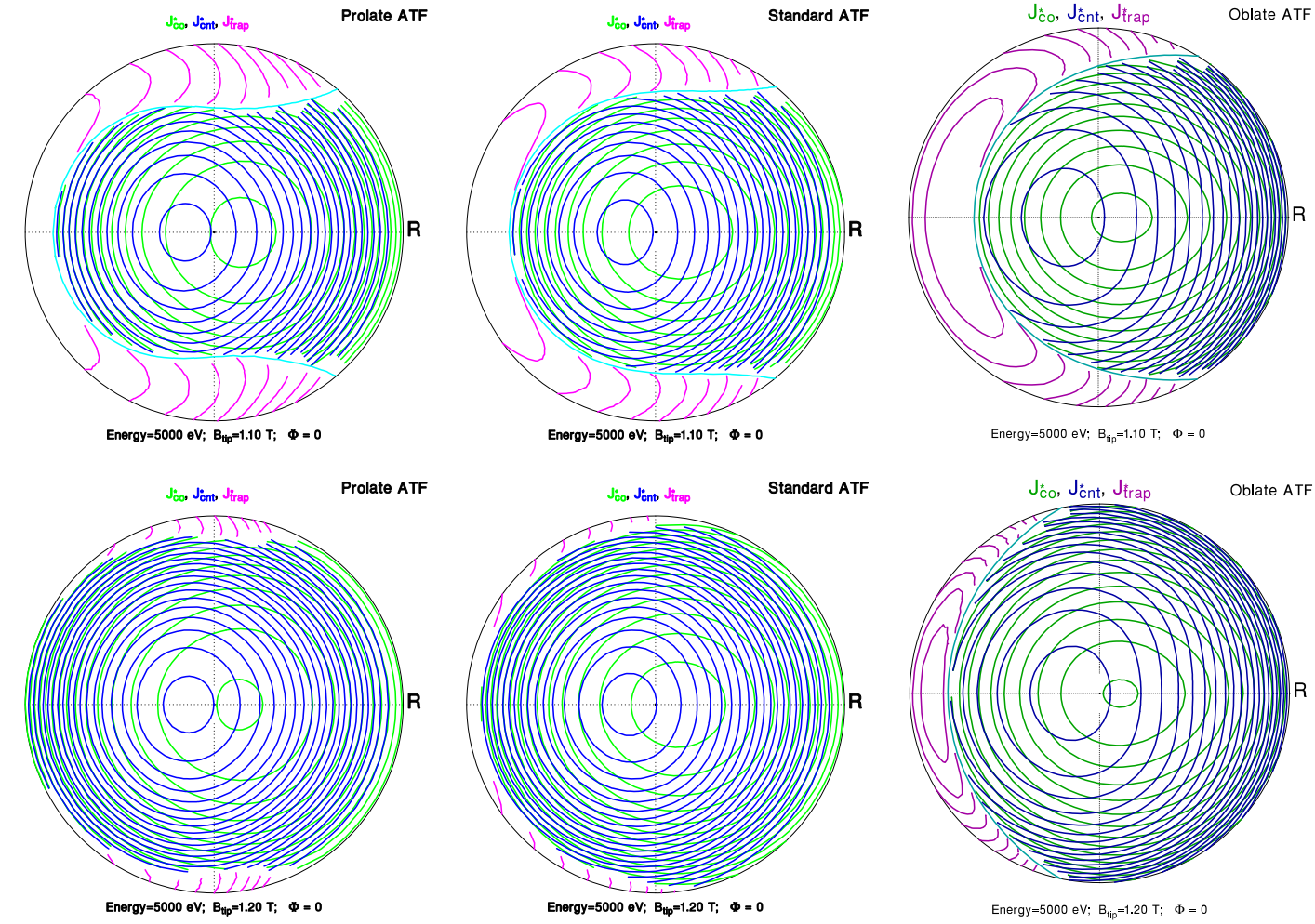

FIG. 9 (Second Part). Orbit topology for 5 keV protons in ATF with no radial electric field for the three configurations of Table I.

of B in the plasma, because in this regime, no orbit can become trapped. Accordingly, all of the features of the orbit topology for the ATF cases can be encountered in a quite narrow range of B_{tip}, $0.9 < B_{tip} < 1.2$. At lower values of B_{tip}, the entire region becomes forbidden, or else no helically trapped orbits are contained. At higher values of B_{tip}, all the orbits are circulating.

The entire orbit topology for the three ATF configurations with no radial electric field is shown in Fig. 9. According to the size of the last closed B_{min} contour, the best case should be the oblate configuration, and the worst case should be the prolate configuration. This conclusion is reflected in the upper two rows of plots since the B_{min} contours surround the forbidden regions. In the oblate case, the forbidden region has pulled away from the inner wall, and there are more helically trapped orbits contained. The middle three rows examine the behaviour of the transitional orbits. Only the oblate case has any significant number of transitional orbits contained. The bottom row shows mostly circulating orbits. The counter-circulating orbits have more of a tendency to either hit the wall or to encounter the trapping boundary; co-circulating orbits are better contained.

The fact that, for all the configurations, almost all of the transitional orbits are lost (at an energy of 5 keV) is a source of concern for heating the plasma ions with tangential neutral beam injection (NBI) or ion cyclotron radio-frequency (ICRF) heating. Above the critical energy ($E_{crit} = 14.8\,T_e$), the injected or heated ions transfer most of their energy to electrons. Below E_{crit}, the ions rapidly pitch angle scatter and will be lost when they become trapped. ICRF minority heating interacts with the deeply trapped ions in the tail of the distribution function. The region of contained trapped ions is near the inner edge of the plasma, far from antennas placed in outer ports, making coupling difficult. Any perpendicular energy delivered to untrapped ions will cause them to become trapped, and they will also hit the wall at the trapped–passing transition boundary.

However, the situation changes when a radial electric field is added.

7. J^* TOPOLOGY — WITH ELECTRIC FIELD

In general, stellarators and tokamaks have been shown to operate with radial potentials that are on the order of the plasma temperature. The ATF experiment is capable of

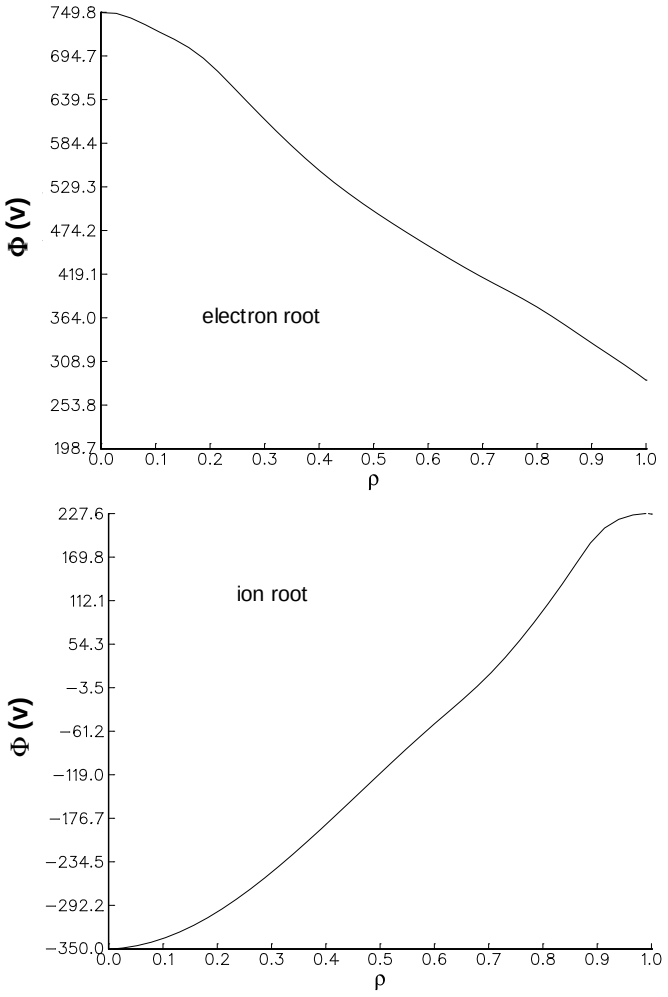

FIG. 10. Fits to the measured potential profiles in ATF under ECH heating (top) and NBI heating (bottom).

measuring the potential over most of the plasma. A heavy-ion beam probe diagnostic from Renesselaer Polytechnic Institute is used for the centre, and a reciprocating Langmuir probe (in co-operation with the University of Texas, Austin) at the edge. For this study, two experimental potential profiles (Fig. 10) were measured by S. Aceto (R.P.I.) [11] that have been smoothly continued to the centre of the plasma. Two cases are used: in a low density ECH-heated plasma, the potential acted to contain electrons (electron root); and in an NBI-heated case, the potential acted to contain ions (ion root). The potential measured in the NBI case has not been corrected for probable UV loading errors [12] owingto the extremely l imited NBI operating time on ATF during 1991.

Our ion orbit scans (Fig. 11) are performed at constant total energy, so if the electrostatic potential becomes too large, $E - \mu B - e\Phi$ will become less than zero, and orbits (at the particular value of B_{tip}) will be forbidden. In the electron root case, the forbidden region occurs in the centre of the plasma; in the ion root case, it occurs near the edge. The most deeply trapped orbit hugs the edge of the forbidden region just as in the case with no electric field. Accordingly, the remarkable result is that the trapped orbits are contained inside the circulating orbits in the electron root case. Since the deviation of the circulating orbits from a flux surface is small, the loss region is mostly healed. The ion root case is more conventional: the forbidden region is at the edge of the plasma, and the ions are contained electrostatically by it.

The energy of a 1 keV ion is about twice the above measured potentials. Unfortunately, as the energy is increased, there is inevitably a place where the poloidal $\boldsymbol{E} \times \boldsymbol{B}$ velocity cancels out the slow poloidal precession of the helically trapped orbits, and resonance occurs with resulting direct loss of particles. This situation is found in many devices (e.g., the Elmo Bumpy Torus) and depends strongly on the shear in the electric field. The good confinement of transitional orbits disappears by the time the energy reaches 3 keV, as shown in Figs 12 and 13.

8. IMPLICATIONS OF RESULTS

ATF was designed to optimize MHD properties to achieve stable entry into the second-stability regime, and not to minimize orbit losses. It was believed that the naturally occurring electric field would heal the loss regions for the particles in the thermal distribution function; as Fig. 11 shows, this assumption was correct.

The difficulty occurs when auxiliary heating is considered. ATF has three types available: ECH, ICRF and NBI. ECH works very well in ATF since the heated electrons rapidly transfer their energy to the bulk plasma. Unfortunately, ECH is quite expensive, and the plasma density is limited by the cut-off frequency.

Neutral beam injectors are aimed tangentially in ATF (co + counter). The fast (~45 keV) protons are born circulating and are reasonably well contained in ATF. Above the critical energy (14.8 T_e), the fast ions slow down on the plasma electrons without pitch angle scattering. However, when pitch angle scattering starts to occur, the fast ions must cross the large loss region at the trapped–passing boundary, and many of these ions are lost before they can transfer their energy directly to ions. Therefore, it is difficult to heat ions directly via NBI in ATF [13]. At high plasma densities ($\bar{n}_e \sim 10^{14}$ cm^{-3}), T_e is low and the electron–ion coupling is high so that the beam energy can be transferred to the ions via the electrons. But at moderate densities, ECH still cannot penetrate to the core of the plasma, and the beam energy is not well coupled to the ions via the electrons, thus the ion temperature remains low.

Minority ICRF heating in ATF also presents problems. The minority ions form a tail in the perpendicular region of velocity space, much of which is in the loss region (Figs 12 and 13). In addition, ICRF tends to increase the perpendicular energy of the heated ions, so they become more deeply trapped. Contained deeply trapped ions are never

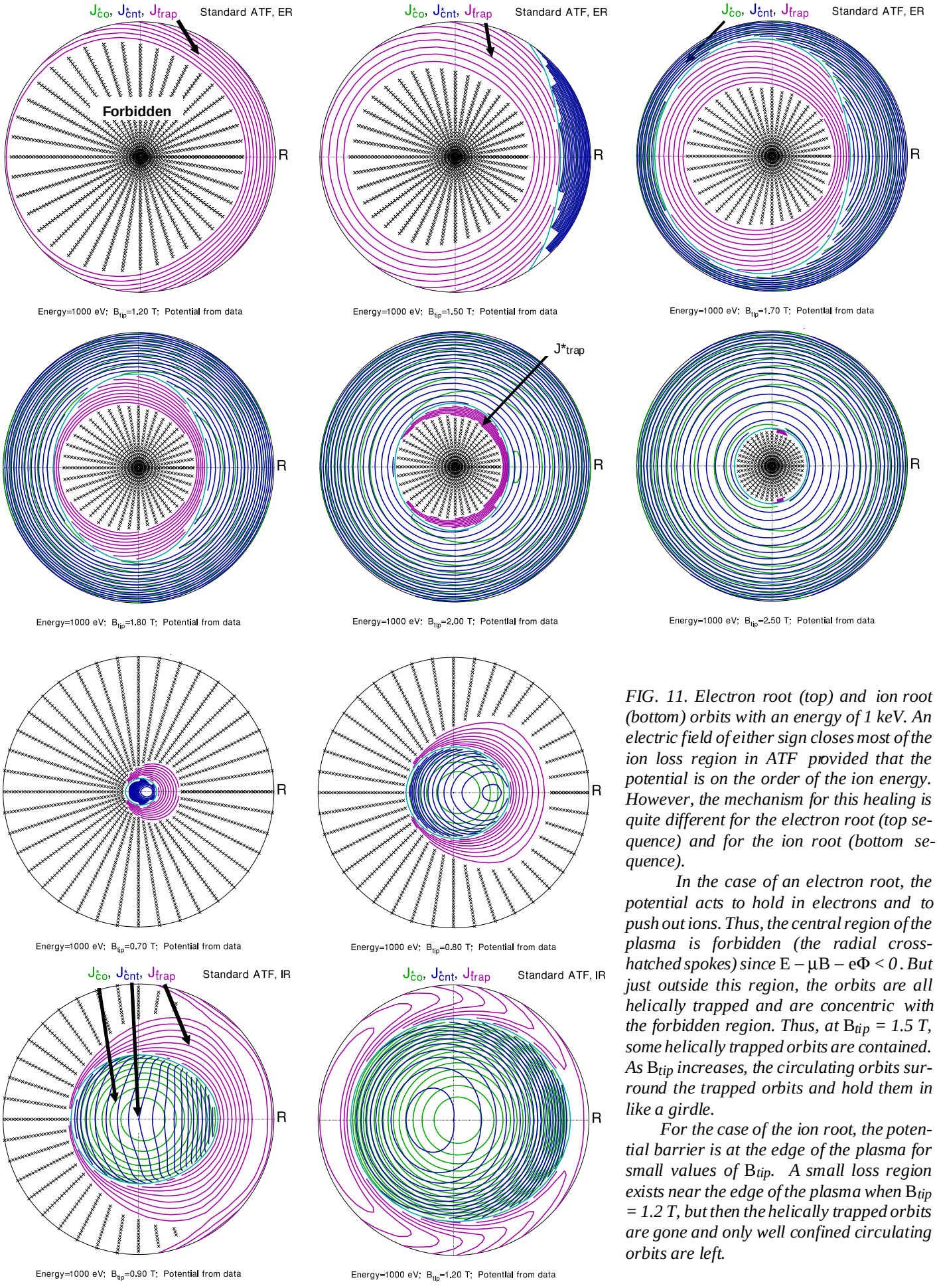

FIG. 11. Electron root (top) and ion root (bottom) orbits with an energy of 1 keV. An electric field of either sign closes most of the ion loss region in ATF provided that the potential is on the order of the ion energy. However, the mechanism for this healing is quite different for the electron root (top sequence) and for the ion root (bottom sequence).

In the case of an electron root, the potential acts to hold in electrons and to push out ions. Thus, the central region of the plasma is forbidden (the radial cross-hatched spokes) since $E - \mu B - e\Phi < 0$. *But just outside this region, the orbits are all helically trapped and are concentric with the forbidden region. Thus, at* $B_{tip} = 1.5$ *T, some helically trapped orbits are contained. As* B_{tip} *increases, the circulating orbits surround the trapped orbits and hold them in like a girdle.*

For the case of the ion root, the potential barrier is at the edge of the plasma for small values of B_{tip}. *A small loss region exists near the edge of the plasma when* $B_{tip} = 1.2$ *T, but then the helically trapped orbits are gone and only well confined circulating orbits are left.*

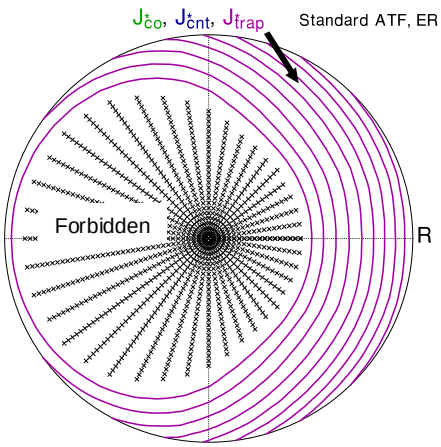

Energy=3000 eV; B_{tip}=1.00 T; Potential from data

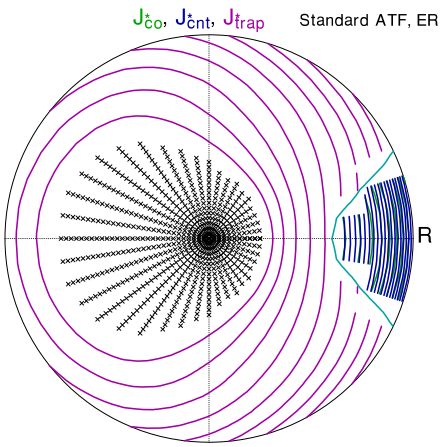

Energy=3000 eV; B_{tip}=1.10 T; Potential from data

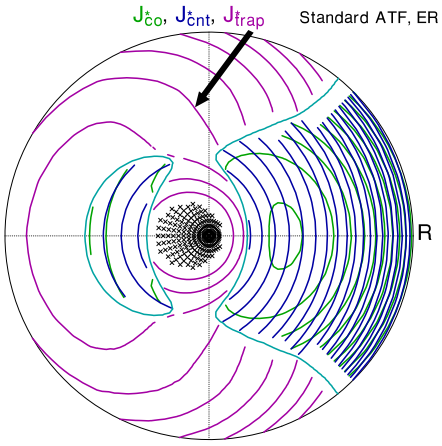

Energy=3000 eV; B_{tip}=1.20 T; Potential from data

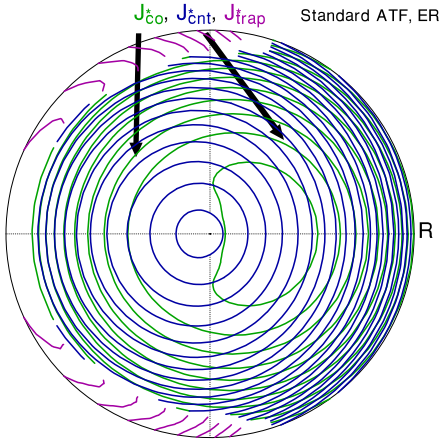

Energy=3000 eV; B_{tip}=1.30 T; Potential from data

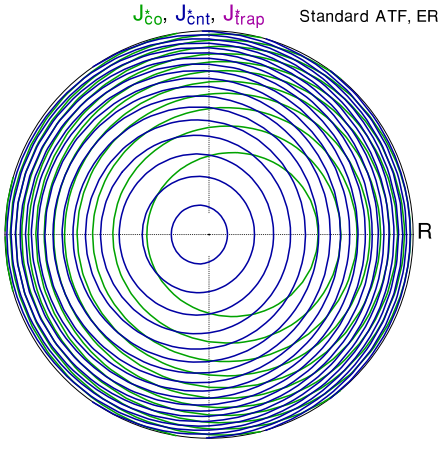

Energy=3000 eV; B_{tip}=1.50 T; Potential from data

FIG. 12. Electron root orbits at 3 keV still show a severe loss region at the trapped–passing boundary. From B_{tip} = 1.1–1.3 T, almost all transitional orbits are lost. The only exception occurs for the bizarre case when B_{tip} = 1.2 T. Near the centre, there are a few orbits with inside bananas and outside bananas that are joined by helically trapped sections and encircle the electrostatically forbidden region in the centre. And, almost all of the helically trapped (non-transitional orbits) are in the loss region also.

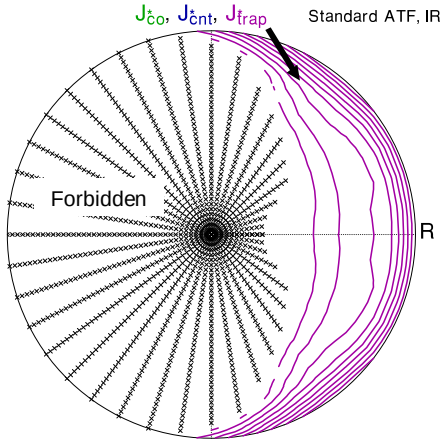

Energy=3000 eV; B_{tip}=0.80 T; Potential from data

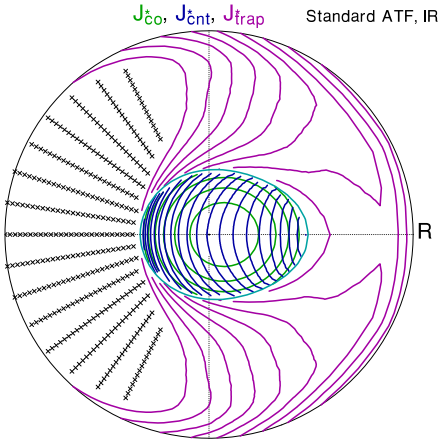

Energy=3000 eV; B_{tip}=0.90 T; Potential from data

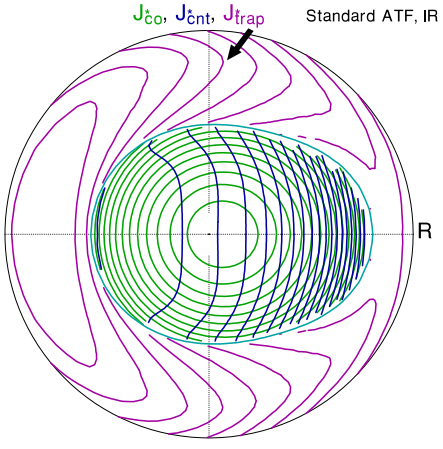

Energy=3000 eV; B_{tip}=1.00 T; Potential from data

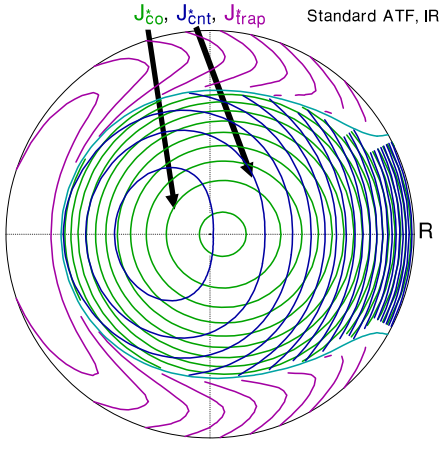

Energy=3000 eV; B_{tip}=1.10 T; Potential from data

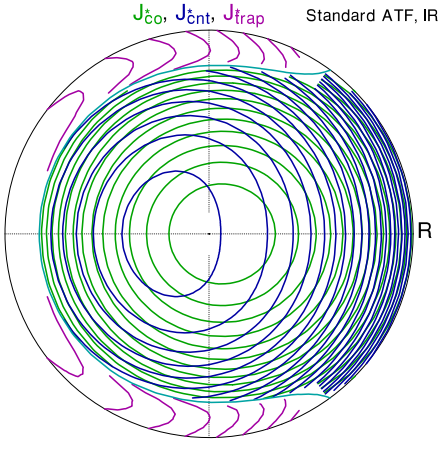

Energy=3000 eV; B_{tip}=1.20 T; Potential from data

FIG. 13. Ion root orbits at 3 keV also show a severe loss region at the trapped–passing boundary. All transitional orbits are lost. The few contained helically trapped orbits are near the inside edge of the plasma.

found at the outside edge of the plasma, making coupling to the ATF antenna (which is in an outside port) more difficult.

Because ICH is a cheap and long-pulse heating technology, it is of interest to try and evade the above problems. One method is to use direct electron heating which has been successful on TFTR [14, 15]. Another is to try and find a mechanism for heating the bulk ions directly, perhaps with ion Bernstein or lower hybrid waves, a subject of some speculation, but little success.

The ATF configuration is flexible, and there are configurations that provide better particle containment. For example, pushing the magnetic axis inward improved the confinement at the expense of MHD stability. However, as beta increases, the ATF configuration digs a magnetic well and becomes more stable, so one operation scenario could be to push the magnetic axis inward as beta increases. However, we have also studied the orbits corresponding to Figs 12 and 13 for the oblate and prolate configurations of ATF, and no noticeable improvement was obtained theoretically. Experiments on ATF that varied the configuration showed that, if anything, the prolate configuration yielded a higher stored energy, but too many factors changed between the cases to draw firm conclusions.

In addition, we looked at several cases with moderate values of beta (several per cent). If the vertical field is increased to keep the magnetic axis at approximately the same position, the orbit topology is qualitatively the same as it is in the low beta case. If the magnetic axis is allowed to move outward with increasing beta, the loss region becomes worse as would be expected.

9. CONCLUSIONS

This paper has shown that the use of the J^* invariant provides a fast and reliable method to see the totality of the orbits in any given configuration. The most bizarre orbits that are predicted by these plots can be found using a guiding centre orbit code. In addition, we have emphasized the importance of the use of symplectic integration to provide reliable orbits over long integration times.

We applied the J^* method to the case of ATF and found that the loss regions that exist without a radial electric field are healed by a potential of about half the particle energy. However, the loss regions are moved to higher energies and can intercept the superthermal ions produced by NBI or ICH. As a result, heating the ion distribution in ATF from above is difficult, and schemes that interact directly with the bulk thermal distribution are preferred.

ACKNOWLEDGEMENTS

The author wishes to thank John Cary of the University of Colorado, Boulder, for his symplectic integrator, work on J^*, and useful advice. C. Lewis Hedrick of Oak Ridge National Laboratory (ORNL) also pioneered work on the use of J^* helped clarify many issues and acted as a sounding board for many speculations. Other useful discussions were held with Jeffrey Harris, James Lyon, Mickey Wade and David Rasmussen, all of ORNL; Allen Boozer of William and Mary; and Steve Aceto of Renesselaer Polytechnic Institution. This research was sponsored by the Office of Fusion Energy, US Department of Energy, under contract DE-AC05-84OR21400 with Martin Marietta Energy Systems, Inc.

REFERENCES

[1] NÜHRENBERG, J., ZILLE, R., Phys. Lett., **A114** (1986) 129.
[2] CARY, J.R., et al., Phys. Fluids **31** (1988) 1586.
[3] ROME, J.A., PENG, Y.-K. M., Nucl. Fusion **19** (1979) 1193.
[4] BOOZER, A.H., Phys. Fluids **23** (1980) 904.
[5] KUO-PETRAVIC, G., et al., J. Comput. Phys. **51** (1983) 261.
[6] FOWLER, R.H., et al., Phys. Fluids **28** (1985) 338.
[7] HIRSHMAN, S.P., et al., Comput. Phys. Comm. **43** (1986) 143.
[8] LYON, J.F., et al., Fusion Technol. **17** (1990) 33.
[9] CARY, J.R., Bull. Am. Phys. Soc. **34** (1989) 1927.
[10] HALL, L.S., McNAMARA, B., Phys. Fluids **18** (1975) 552.
[11] ACETO, S.C., Measurement of the Radial Electric Field in the Advaced Toroidal Facility using a Heavy Ion Beam Probe, PhD Thesis, Dept. of Physics, Renesselaer Polytechnic Institute, Renesselaer (1993).
[12] MATHEW, J., Rev. Sci. Instrum. **51** (1985) 987.
[13] WADE, M.R., An Experimental Study of Ion Behavior in the Advanced Toroidal Facility, PhD Thesis, Georgia Institute of Technology, Atlanta (1991).
[14] PETTY, C.C., et al., in Radio Frequency Power in Plasmas (Ninth Top. Conf. Charleston, 1991), AIP Conf. Proc. **244** (1992) 96.
[15] MURAKAMI, M., et al., in Radio Frequency Power in Plasmas (Tenth Top. Conf. Boston, 1993), AIP Conf. Proc. **289** (1994) 48.

(Manuscript received 28 December 1994
Final manuscript received 27 April 1994)